

Finite difference time domain modelling of sound scattering by the dynamically rough surface of a turbulent open channel flow



Kirill V. Horoshenkov^{a,*}, Timothy Van Renterghem^b, Andrew Nichols^c, Anton Krynkina^a

^a Department of Mechanical Engineering, University of Sheffield, Mappin Street, Sheffield S1 3JD, UK

^b Department of Information Technology, Ghent University, St.-Pietersnieuwstraat 41, 9000 Gent, Belgium

^c Department of Civil and Structural Engineering, University of Sheffield, Mappin Street, Sheffield S1 3JD, UK

ARTICLE INFO

Article history:

Received 11 December 2015

Received in revised form 11 March 2016

Accepted 16 March 2016

Keywords:

Sound scattering
Rough surface
Acoustic modelling
Turbulent flow

ABSTRACT

The problem of scattering of airborne sound by a dynamically rough surface of a turbulent, open channel flow is poorly understood. In this work, a laser-induced fluorescence (LIF) technique is used to capture accurately a representative number of the instantaneous elevations of the dynamically rough surface of 6 turbulent, subcritical flows in a rectangular flume with Reynolds numbers of $10,800 \leq Re \leq 47,300$ and Froude numbers of $0.36 \leq Fr \leq 0.69$. The surface elevation data were then used in a finite difference time domain (FDTD) model to predict the directivity pattern of the airborne sound pressure scattered by the dynamically rough flow surface. The predictions obtained with the FDTD model were compared against the sound pressure data measured in the flume and against that obtained with the Kirchhoff approximation. It is shown that the FDTD model agrees with the measured data within 22.3%. The agreement between the FDTD model and stationary phase approximation based on Kirchhoff integral is within 3%. The novelty of this work is in the direct use of the LIF data and FDTD model to predict the directivity pattern of the airborne sound pressure scattered by the flow surface. This work is aimed to inform the design of acoustic instrumentation for non-invasive measurements of hydraulic processes in rivers and in partially filled pipes.

© 2016 The Authors. Published by Elsevier Ltd. This is an open access article under the CC BY license (<http://creativecommons.org/licenses/by/4.0/>).

1. Introduction

Turbulent, depth-limited flows such as those in natural rivers and urban drainage systems always have patterns of waves on the air/water boundary which carry information about the mean flow velocity, depth, turbulent mixing and energy losses within that flow. Monitoring of these flows is vital to predict accurately the timing and extend of floods, manage natural water resources, operate efficiently and safely waste water processing plants and manage underground sewer networks.

Given the importance of these types of flows, it is surprising that there are no reliable methods or instruments to measure the shallow water flow characteristics in the laboratory or in the field remotely. The majority of existing instrumentation for flow measurements needs to be submerged under water and provides only local and often inaccurate information on the true flow characteristics such as the flow velocity and depth [1]. The submerged instrumentation is often unable to operate continuously over a long period of time because it is prone to damage by flowing debris

and its battery life is limited. Currently, it is impossible to measure remotely and in-situ the flow mixing ability, turbulence kinetic energy, Reynolds stress, sediment erosion rates and the volume fraction of suspended/transported sediment. These characteristics are essential to calibrate accurately the existing and new computational fluid dynamics models, implement efficient real time control algorithms, forecast flooding and to estimate the potential impact of climate change on water infrastructure and the environment. Equally, there are no reliable and inexpensive laboratory methods to measure a flow over a representatively large area of a flume or partially filled pipe so that spatial and temporal flow characteristics predicted by a model can be carefully validated. The widely used particle image velocimetry [2] or LiDAR methods are notoriously expensive and difficult to set up, calibrate and make work to cover a representative area of flow either in the laboratory [3] or in the field [4].

In this sense, accurate data on the flow surface pattern characteristics are important. Recent work [5,6] suggests that there is a clear link between the statistical and spectral characteristics of the dynamic pattern of the free flow surface and characteristics of the underlying hydraulic processes in the flow. More specifically, the work by Horoshenkov et al. [5] showed that the mean

* Corresponding author.

roughness height, characteristic spatial period and correlation length are related to the mean flow depth, velocity and hydraulic roughness coefficient. The work by Nichols [6] showed that the characteristic spatial period of the dynamic surface roughness is related to the scale of the turbulence structures which cause the surface to appear rough.

In this sense the use of airborne acoustic waves to interrogate the flow surface to determine some of the key characteristics of the dynamic surface roughness is attractive to measure the in-flow processes remotely. Radio (e.g. [7]) and underwater acoustic waves (e.g. [8]) have been used extensively since the last century to measure the statistical and spectral characteristics of the sea and ocean waves. Doppler radar methods were used to estimate the velocity of rivers (e.g. [9]). However, these methods have not been used widely to measure the roughness in rivers and other open channel flows, which is surprising given the importance of a good understanding of the behaviour of these types of natural hydraulic environments. In this respect, the development of non-invasive instrumentation for the characterisation of open channel flows is impeded by the lack of understanding of the roughness patterns which develop on the surface of these types of flows and ability to model the wave scattering by these surface roughness patterns. Therefore, the purpose of this paper is to study the application of the FDTD technique to predict the time-dependent acoustic wave scattering patterns, and their directivity, which are observed above the dynamically rough surface of a turbulent, shallow water flow.

The paper is organised in the following manner. Section 2 presents the experimental facility which was used to measure the acoustic scattering patterns for a range of hydraulic flow conditions. Section 3 presents the modelling methodologies. The results and discussion are presented in Section 4.

2. Experimental method and data pre-processing

2.1. Flow conditions

For this work, the rough surfaces to be used for validating the acoustic models were generated by a turbulent flow. The hydraulic conditions studied in this work were designed to generate a number of different dynamic water surface patterns for a number of flow conditions as detailed in Table 1. Experiments were carried out in a 12.6 m long, 0.459 m wide sloping rectangular flume (see Fig. 1) which is available in the University of Bradford. The flume had a bed of hexagonally packed spheres with a diameter of 25 mm, and was tilted to a slope of $S_0 = 0.004$.

The depth of the flow was controlled with an adjustable gate at the downstream end of the flume to ensure uniform flow conditions throughout the measurement section. The uniform flow depth relative to the bed was measured with point gauges that were accurate to the nearest 0.5 mm (between 0.6% and 1.2% of the flow depths used). This was conducted at 4 positions, situated 4.4–10.4 m from the upstream flume end in 2 m increments, with uniform flow being confirmed when the values agreed to within

0.5 mm of each other. This meant that the flow was not spatially changing, i.e. no net acceleration or deceleration across the measurement frame, so that the statistical properties of the free surface roughness were uniform across the measurement area.

The uniform flow depth, D , was varied from 40 mm to 90 mm by adjusting the flow rate using a control valve in the supply pipe, and a downstream gate was to ensure uniform flow. The flow rate, Q , was measured via a calibrated orifice plate, and varied from 5 l/s to 27 l/s. The resulting mean flow velocity, U , varied from 0.28 m/s to 0.65 m/s. The Froude number for these flows ranged from 0.36 to 0.69, such that all flows were subcritical, and Reynolds number ranged from 10,800 to 47,300 so that all flows can be considered turbulent. Table 1 presents a summary of the hydraulic conditions realised in the reported experiments. A photograph of an example of the flow surface roughness observed in flow condition 1 is shown in Fig. 2.

2.2. Free-surface position measurement

A laser induced fluorescence (LIF) technique was employed to measure the free-surface position in a vertical plane along the centreline of the flume at the test section. A diagram of the LIF arrangement for the flow surface measurement is shown in Fig. 3. A sheet of laser light was projected vertically through the flow surface, and a high-resolution camera was used to image the intersection between the laser sheet and the water surface.

An optical system was used to form and focus the laser light sheet, which illuminated a volume approximately 250 mm long in the streamwise direction and approximately 3 mm thick in the lateral direction. In order to define the free-surface clearly in the images, Rhodamine B dye was added to the flow. When illuminated with 532 nm laser light, the Rhodamine is excited, and emits light at around 595 nm. A high-pass filter lens with a cut-off wavelength of 545 nm was used to discard the ambient green (532 nm) light, but allow through the red (595 nm) light emitted by the rhodamine in the water.

The camera was installed at an elevated position, looking down towards the water surface at an angle of 15° (see Fig. 3). This setup allowed for a clear line-of-sight between the surface profile and the camera, with no opportunity for higher water surface features in front of the laser plane to obstruct the view. The camera was calibrated by capturing images of a grid of dots placed in the same plane as the laser. This enabled a direct linear transform to be calculated so that the true position of each image pixel could be determined. This enabled the position of the air–water interface to be detected for each of the 1600 columns of pixels in the recorded images. Images were captured at a fixed frequency of 26.9 Hz. For each flow condition, images were recorded for 5 min, generating a time series of 8070 images.

The images from the LIF camera were used to determine the position of the free surface from each image by detecting the threshold between the illuminated flow and non-illuminated air for each column of pixels. Fig. 4 shows the following analysis steps applied to one instantaneous image from flow condition 4. Firstly, a raw image was loaded (Fig. 4(a)). Secondly, the image pixels were binarized by setting a threshold illumination value above which a pixel was defined as fluorescing water, and below which a pixel was defined as non-fluorescing air (Fig. 4(b)). The quality of the output data was found sensitive to this threshold and so it was determined manually for each flow condition to ensure that the binarized images closely matched the raw images. Thirdly, a 5×5 two-dimensional median filter was applied to remove spurious points of brightness within the air phase or points of darkness in the water phase (Fig. 4(c)). This replaced each value with the median value of the 5×5 grid of logical values surrounding it. Each pixel column was then analysed to determine the pixel location at

Table 1
Measured hydraulic conditions.

Flow condition	Bed slope S	Depth D (mm)	Flow rate Q (l/s)	Velocity U (m/s)	Reynolds number Re
1	0.004	40	5.0	0.28	10,800
2	0.004	50	8.5	0.36	15,100
3	0.004	60	12.0	0.43	24,500
4	0.004	70	16.0	0.50	32,700
5	0.004	80	21.0	0.57	38,800
6	0.004	90	27.0	0.65	47,300

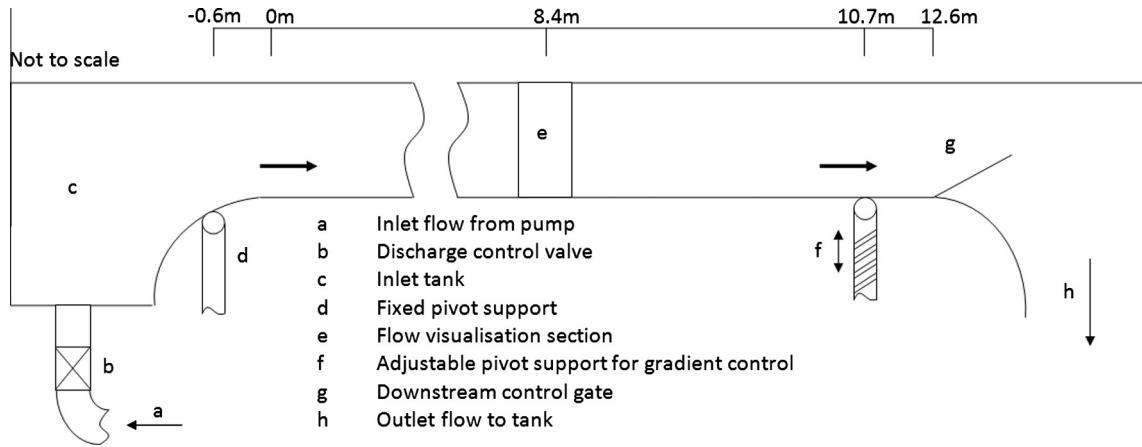


Fig. 1. The overview of hydraulic instrumentation (adapted from [5]).



Fig. 2. A photograph of the flow surface for flow condition 1 showing a range of scales of free surface roughness.

which the air–water interface was located, i.e. when the logical pixel value changed from zero to unity. Fourthly, a 31-pixel wide median filter was applied to remove small fluctuations associated with noise generated by random variation in light levels at the free surface. This operated in the same manner as the previously described median filter, but with a grid size of 31×1 . The width of 31 pixels represents a physical length less than 4 mm, and was the smallest window that produced a smooth profile that visually matched the raw images with no spurious deviations. This length is also much smaller than the typical length scales of the surface roughness pattern and of typical coherent flow structures in depth-limited flows [5]. The result of this procedure is shown on

the original image to illustrate the effectiveness of the technique (Fig. 4(d)). Finally, the calibration was used to convert pixels to millimetres, giving a horizontal and vertical resolution of 0.15 mm as shown in Fig. 4(e). The accuracy of this method was assessed via measurement of a still water surface allowed to settle for 2 h, which showed a maximum fluctuation of ± 0.5 pixels or 75 μm . This variation can potentially reflect remaining oscillations in the water body, nevertheless the maximum error is defined as $\pm 75 \mu\text{m}$. This process was then applied to each of the 500 images acquired for each of the 6 flow conditions examined. These images were randomly selected from the 8070 images acquired through the LIF experiment for each of the flow conditions studied in this work. For each condition this resulted in a time series of surface profile, allowing the examination of surface behaviour over time and space with a high spatial and temporal resolution.

2.3. Acoustic measurements

The acoustic system was installed at the centre of the flume and at 8.4 m from its upstream end, coinciding in position with the flow visualisation section (see Fig. 1). A semi-circular arch-shaped acoustic rig was constructed in order to precisely control the positioning of each of the acoustic components (see Fig. 5). The arch was supported at each corner by a screw thread, allowing the height to be accurately adjusted. The base of the arch was thereby fixed at a distance of 10 mm above the mean water level. A 70 mm diameter ultrasonic transducer (Pro-Wave ceramic type 043SR750) was driven at the frequency of 43 kHz. It was positioned at an angle of 45° to the mean water surface elevation, at

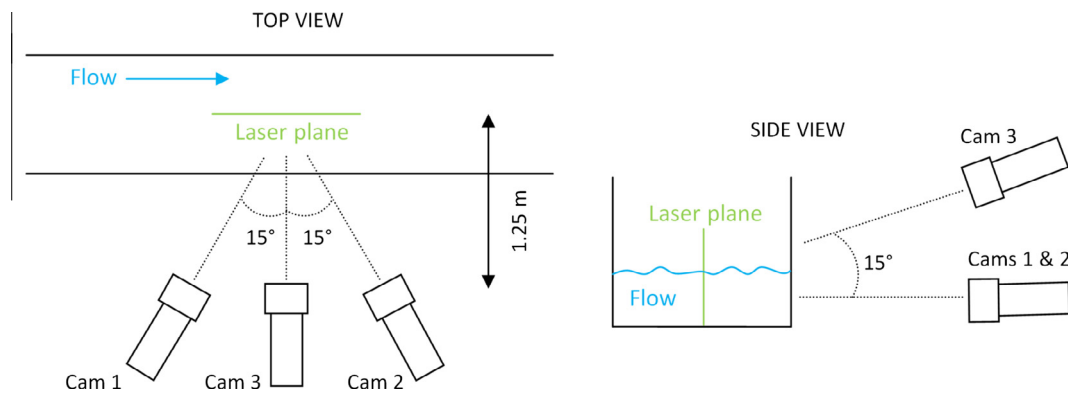


Fig. 3. Diagram of camera arrangements for flow visualisation.

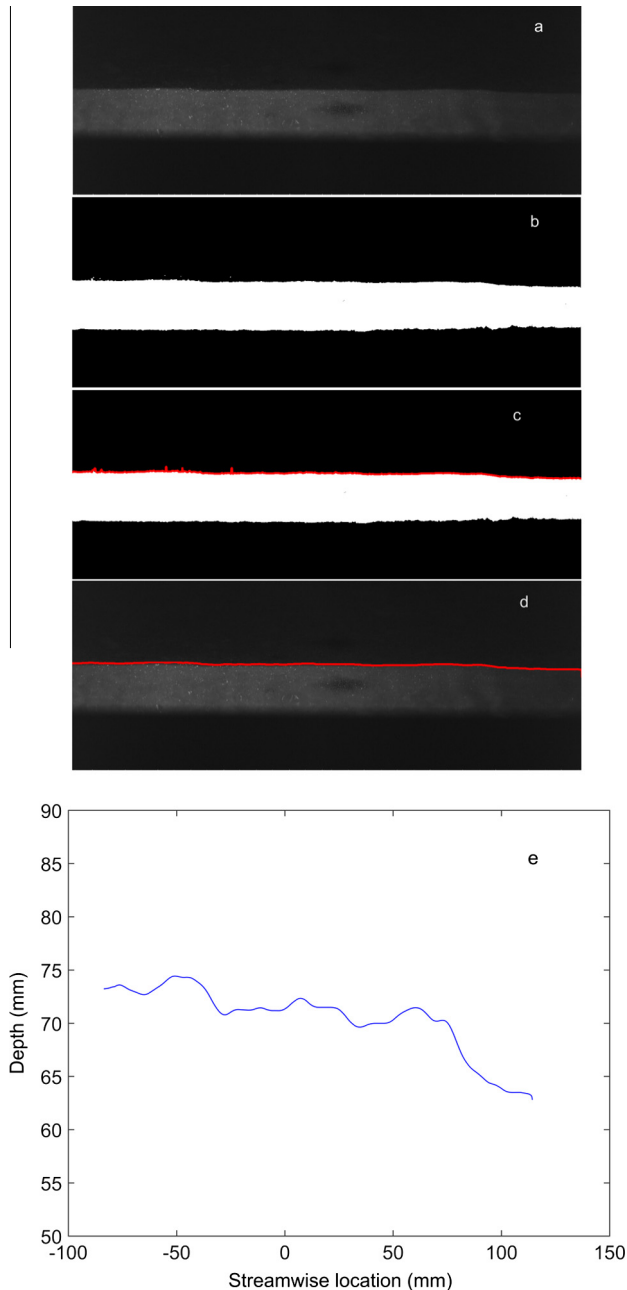


Fig. 4. The pre-processing procedure for laser-induced fluorescence data.

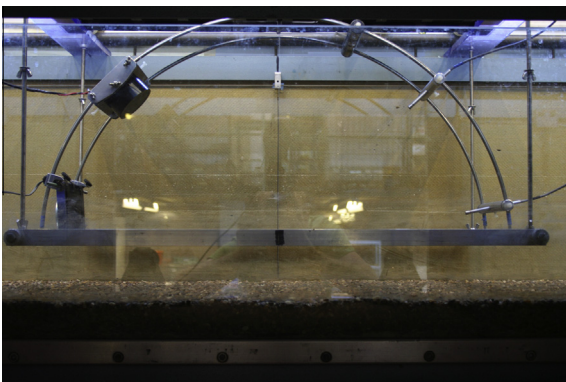


Fig. 5. Support arch for acoustic components. The 70 mm diameter transducer (43 kHz) is on the left, the 1/4" microphones are on the right.

a distance of 0.4 m from the point of incidence. This type of transducer was used in order to achieve a relatively directional acoustic beam ($\pm 6^\circ$ for 6 dB drop-off) to avoid reflection from the nearby flume walls and other objects, and also due to the low noise at ultrasonic frequencies (the signal to noise ratio here was 113 dB).

Four calibrated Brüel & Kjær (B&K) 1/4" type 4930 microphones were placed on the opposite side of the support arch, also at a distance of 0.4 m from the arch centre-point point as shown in Fig. 5. The operating frequency range of these microphones is 4–100,000 Hz, with a sensitivity of 4 mV/Pa. Acoustic readings were taken at 40 different angular positions from 16.4° to 73.6° in 1.4° increments.

The acoustic equipment was designed such that the LIF laser was not obstructed, and nor was the field of view of the flow visualisation camera, allowing the acoustic, and LIF measurements to be recorded simultaneously. The ultrasonic transducer was excited at its resonant frequency in order to produce a continuous sine wave. The signal was provided by a Tektronix AFG 3021B function generator, while the microphone signal was received by a B&K Nexus four-channel microphone conditioning amplifier. The output sensitivity of the Nexus amplifier was set to 100 mV/Pa, such that the output level was close to the data acquisition limit of ± 10 V, without saturating, in order to make use of the maximum resolution possible.

The Nexus amplifier provided an analogue voltage output which was proportional to the instantaneous sound pressure at the microphone. Hence, a data acquisition system was selected which was capable of recording analogue voltage signals between ± 10 V. A National Instruments (NI) PXIe 1062Q chassis was installed with an NI PXIe-6356 data acquisition (DAQ) card capable of simultaneous measurement on up to 8 channels at up to 1.25 MHz sampling rate. For easy connection of the devices, an NI BNC-2110 input board was used. Simple, reliable BNC cables could then be connected between the wave monitor and Nexus units and the DAQ input board.

A National Instruments LabView virtual instrument program was written to record the acoustic signal at 1 MHz sampling rate. The data acquisition was carried out in 1 ms packets to avoid memory overflow. These packets of data were recorded synchronously on all four microphones, and the acquisition of each packet was triggered at a rate of 100 Hz. The resulting raw data were saved into text files so that analysis could be performed using Matlab. The mean time-dependent signal amplitude was then calculated for each packet, and the time series of signal amplitude was averaged over time. This resulted in a time averaged directivity pattern recorded around an arc on the side of the supporting arch opposite the sound source.

3. Modelling methodology

3.1. Finite differences time domain modelling of the acoustic scattering phenomenon

The sound propagation problem from a directional source and in the presence of a rough water surface was solved numerically. Fig. 6 presents schematically the setup used in the simulation. The positions of the source and receivers were selected to reproduce the experimental setup described in Section 2.3. The full-wave finite differences time domain modelling (FDTD) technique was used to numerically solve the two-dimensional sound propagation equations in a still, lossless and homogeneous medium (air) which filled the space above the rough water surface. The efficient pressure–velocity (p - v) staggered-in-space (SIP) staggered-in-time (SIT) numerical discretisation approach [10] was used to explicitly simulate scattering of the sound wave by a set of 500

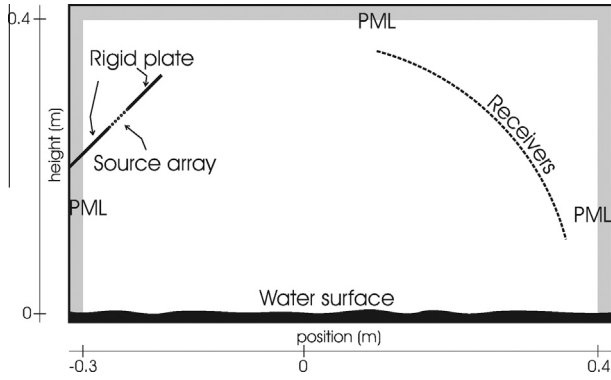


Fig. 6. Schematic setup of the FDTD simulation domain and its dimensions.

surface profile realisations which were measured with the LIF technique which is detailed in Section 2.2. Based on these snapshots, scattering characteristics of the sound field can be calculated.

A spatial discretisation step of 0.5 mm was chosen, which was a compromise between sufficiently capturing surface variations and limiting computational cost, as a large set of surface realisations was required to determine scattering statistics. The p - ν SIP-SIT FDTD implementation [10] used in this study is based on square cells, and each water surface snapshot was thus represented by the best fitted staircase approach. Numerical tests considering the mean absolute pressure over 200 realisations (in case of flow regime 4) showed that a spatial discretisation step of 0.5 mm gave a relative error of 3.7% compared to halving the cell size (to 0.25 mm). This choice was justified in view of the reduction in computing time by a factor 8 when using the coarser grid. Surface-following coordinates [11] or curvilinear FDTD grids [12] could be an alternative.

The Courant number was set to 1, resulting in a temporal discretisation step of 1.03 μ s, ensuring optimal computing times and maximum phase accuracy while preserving numerical stability [13]. The water surface insonification angle adopted in the experimental setup matched the diagonal of the square cells in the numerical model, which lead to zero phase errors [13] for this particular sound propagation path, as well as for the specular reflection propagation path. The water surface itself was modelled as rigid. Perfectly matched layers (PML) [14] were used as absorbing boundary conditions at the right, left, and upper part of the simulation domain as illustrated in Fig. 6.

A highly directional ultrasound source was used in the experiment. This was simulated by placing a 0.033 m long array consisting of 49 point sources between two perfectly reflecting planes representing an acoustic baffle as illustrated in Fig. 6. The source arrangement adopted in the FDTD simulation enabled us to reproduce the directivity of the real source with the accuracy of 5%. Identical Gaussian pulses were injected simultaneously at each source in the array. The complex pressure at the transducer frequency (43 kHz) was calculated through the Fourier transform of the time histories predicted with the FDTD method at the 121 receiver positions covering the 15–75° range of angles along the arch to reproduce the experimental conditions described in Section 2.3. The use of short acoustic pulses was chosen as this source function strongly reduces the computing time compared to emitting a continuous sine wave, for which averaging over a sufficiently long time is needed to get rid of transition effects. Using 3000 time steps allowed the wave front to pass all receiver positions, meaning 3.09 ms propagation time at a sound speed of 340 m/s.

Although a time domain technique has the potential to simulate surface profile changes during sound wave interaction, a “frozen surface” approach was followed given the limitations in the image capturing frequency of 26.9 Hz. In this work, sound reflection from

500 successive surface realisations obtained with the LIF experimental technique (see Section 2.2) was simulated, meaning that the averaged response over a time period of 18.58 s was calculated for each of the 6 flow conditions.

The LIF scanned part of the water surface was about 0.2 m long (see Section 2.2) and it was centered at the specular reflection point. Since the FDTD simulation area extended beyond the zone scanned with the LIF technique, the remaining parts of the surface required for the FDTD simulation were reconstructed by repeating the scanned profile until the space between the perfectly matching layers was completely filled up with the data (see Fig. 6). In order to avoid jumps at the interface of two repeated surface profiles, the surface elevation data were reversed each time a new data set was added.

In addition, the following operations were performed on the LIF scanned surfaces. Firstly, the linear trend in the LIF data resulting from the channel slope was removed. Secondly, a possible offset in water height during the LIF-scanned period was removed by enforcing a zero-mean water height at each point. Thirdly, each surface undulation profile was divided by the standard deviation at each position to make temporal water depth variations uniform all along the surface, and consequently multiplied by the mean of the standard deviations along the scanned surface to retain the overall water depth variation over time corresponding to a specific flow condition. Fig. 7 presents examples of the time-space dependent surface elevation for conditions 2, 4 and 6 which were used in the FDTD simulation. This figure also presents the sound pressure as a function of time and receiver angle which corresponds to each of these three conditions.

3.2. Stationary wave approximation

The use of stationary phase approximation to predict the averaged acoustic scattering pattern by a dynamically rough open flow surface was proposed in Ref. [15]. This method can be used to avoid the need to evaluate numerically the Kirchhoff integral for the mean sound pressure above the statistically rough rigid surface

$$\overline{p_K(\mathbf{R})} = \frac{1}{4\pi i} \int A(\phi) \frac{e^{ik(R_0+R_1)}}{R_0R_1} q_z e^{-\sigma^2 q_z^2/2} d\mathbf{r} \quad (1)$$

where \mathbf{R} is the vector pointing at the receiver position, $d\mathbf{r}$ is the element of the rough surface pointed at by the vector \mathbf{r} and over which the integral is taken, k is the acoustic wavenumber, $A(\phi)$ is the source directivity as a function of the zenith angle ϕ , R_0 and R_1 are the distances from the source to the rough surface element $d\mathbf{r}$ and from the rough surface element $d\mathbf{r}$ to the receiver, respectively, $q_z = k(z_0/R_0 + z_1/R_1)$, z_0 is the source height above the mean surface level, z_1 is the receiver height above the mean water level and σ is the mean roughness height as it is shown in Fig. 8. Here we refer to the mean roughness height, $\sigma = \sqrt{\frac{1}{M} \sum_m [\eta(t_m) - \bar{\eta}]^2}$, which is a measure of the roughness of the instantaneous surface elevation $\eta(t_m)$, with the mean water level being $\bar{\eta} = \frac{1}{M} \sum_m \eta(t_m) = 0$ and M is the number of samples.

It was shown in [16] that Eq. (1) is accurate if local curvature radius a of the rough surface and acoustic wavelength $\lambda = 2\pi/k$ satisfies the relaxed validity condition of the Kirchhoff approximation, $ka \sin^3 \psi > 1$, where ψ is local angle of incidence. It is noted that for tested flow conditions the Kirchhoff approximation was valid up to a sub-centimetre scale in spatial correlation. Smaller spatial scales that may exist on the surface have higher slopes and are outside of the validity range. However, the contribution of these scales to integral (1) is estimated to be in the second order of smallness of scattering coefficients and should not reduce the accuracy of proposed method by more than 10%. In Ref. [15] it

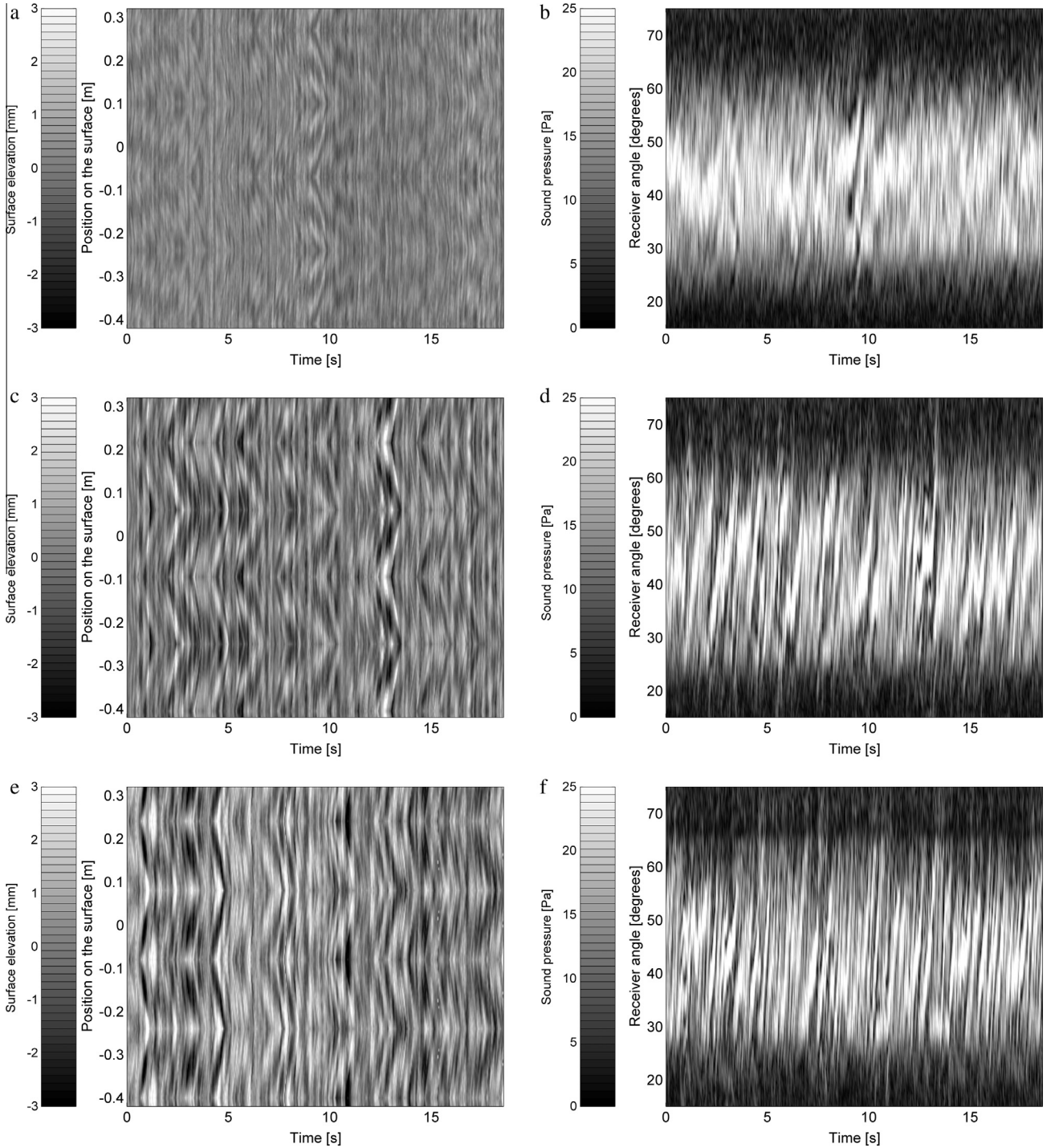


Fig. 7. Examples of the frozen and cyclic extended surface elevation realisations for conditions 2 (top), 4 (middle) and 6 (bottom) and the corresponding dependence of the sound pressure predicted with the FDTD method for the range of receiver angles.

was shown by using the stationary phase approach that integral (1) can be approximated with the following simple expression

$$\overline{p_K(\mathbf{R})} \approx \frac{1}{2k} \frac{f(\mathbf{r}_s)}{\sqrt{|D(\mathbf{r}_s)|}} e^{ik(R_0+R_1) - \sigma^2 q_z^2 / 2} \quad (2)$$

where \mathbf{r}_s is the vector pointing to the position of the specular reflection point on the rough surface, $f(\mathbf{r}_s) = \left[\frac{A(\phi)q_z}{R_0 R_1} \right]_{\mathbf{r}=\mathbf{r}_s}$, $D(\mathbf{r}_s) = \left[\frac{\partial^2 \alpha}{\partial x^2} \frac{\partial^2 \alpha}{\partial y^2} - \left(\frac{\partial^2 \alpha}{\partial x \partial y} \right)^2 \right]_{\mathbf{r}=\mathbf{r}_s}$, $\mathbf{r} = (x, y)$ are the Cartesian coordinates in the plane of the mean water level, and $\alpha(\mathbf{r}_s) = [R_0 + R_1]_{\mathbf{r}=\mathbf{r}_s}$.

In the case when the sound pressure reflected by a flat surface, i.e. when $p_K(\mathbf{R}, \sigma = 0) = p_0(\mathbf{R})$, is known, Eq. (2) reduces to

$$\overline{p_K(\mathbf{R})} \approx \frac{1}{2k} \frac{f(\mathbf{r}_s)}{\sqrt{|D(\mathbf{r}_s)|}} e^{ik(R_0+R_1)} \quad (3)$$

and it is possible to find the ratio of pressures

$$\overline{p_K(\mathbf{R})} / p_0(\mathbf{R}) = e^{-\sigma^2 q_z^2 / 2} \quad (4)$$

from which the mean roughness height can be estimated as

$$\sigma = 1/q_z \sqrt{2 \log(p_0(\mathbf{R}) / \overline{p_K(\mathbf{R})})}. \quad (5)$$

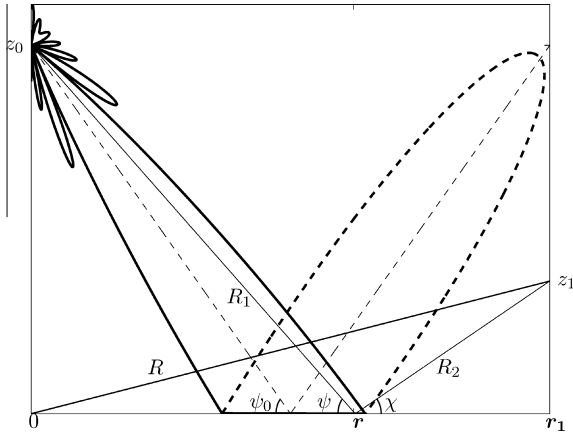


Fig. 8. The geometry of the acoustic setup used for the derivation of the stationary phase approximation (adapted from [15]).

Eq. (5) enables us to estimate the mean surface roughness height by taking the mean sound pressure at a point \mathbf{R} above a dynamically rough surface and then repeating the same measurement with the same source/receiver configuration with respect to the specular reflection point \mathbf{r}_s but in the absence of flow, i.e. when the water is still.

4. Results

The mean amplitude of the sound pressure calculated for the 500 surface realisations with the proposed FDTD method (Section 3.1) was compared against that predicted with the stationary phase approximation (see Section 3.2). The mean amplitude predicted with the FDTD model was calculated as

$$\overline{p(\mathbf{R})} = \left| \frac{1}{M} \sum_{m=1}^M p_m(\mathbf{R}) \right|, \quad (6)$$

where $p_m(\mathbf{R})$ is the complex sound pressure at the position \mathbf{R} corresponding to the m -th surface realisation. A range of positions \mathbf{R} at which the pressure was predicted was chosen to correspond to the positions used in the acoustic experiment which is described in Section 2.3. These corresponded to the range of angles between 15° and 75° . A comparison was made for the 6 hydraulic conditions for which the surface roughness data were measured with the LIF method as detailed in Section 2.2. In the stationary wave approximation we used the values of the mean roughness height listed in Table 2 and the absolute value of the sound pressure, $|p_0(\mathbf{R})|$, predicted with the FDTD method for the flat, perfectly reflecting surface, which were substituted into Eq. (4) to determine $|p_K(\mathbf{R})|$. The value of the mean roughness height for each of the 6 conditions was calculated as

$$\sigma = \frac{1}{N} \sum_{n=1}^N \sigma_n, \quad (7)$$

Table 2
Mean roughness height data and relative errors.

Hydraulic condition	Mean depth, d , mm	Mean roughness height, σ , mm	Relative error, ε_K , %	Relative error, ε_{FDTD} , %
1	40	0.305	2.29	22.3
2	50	0.431	2.80	14.6
3	60	0.698	2.83	17.5
4	70	0.853	1.58	10.7
5	80	1.041	3.03	9.9
6	90	1.112	2.46	10.2

where $\sigma_n = \sqrt{\frac{1}{M} \sum_{m=1}^M [\eta_n(t_m) - d]^2}$ is the time-averaged, root mean square roughness height at the position x_n on the flow surface, $N = 7401$ is the total number of the positions along the surface considered in the FDTD model, $M = 500$ is the number of time points, t_m , at which the instantaneous elevation, $\eta_n(t_m)$, was measured and d is the mean depth as given in Table 2. Fig. 9 shows the comparison of the directivity pattern of the mean value of the modulus of the sound pressure scattered by the rough surface for the six flow condition studied in this work. Table 2 also presents the relative error between the absolute values of the mean sound pressure predicted with the stationary phase approximation and FDTD model. The relative mean error for each of the 6 flow conditions was calculated as

$$\varepsilon_K = \frac{\sum_v v |\overline{p(\mathbf{R}_v)} - \overline{p_K(\mathbf{R}_v)}|}{\sum_v |\overline{p_K(\mathbf{R}_v)}|}, \quad (8)$$

where v is the index covering the range of the receiver positions, \mathbf{R}_v , considered in this work. The results show that the error between the amplitude of the mean sound pressure predicted with the stationary phase approximation and with the FDTD model does not exceed 3.03%. The directivity pattern predicted with the FDTD model is more complex than that predicted by the stationary phase approximation (Eq. (4)). The stationary phase approach takes into account contribution only from a single point on the surface compared to FDTD or Kirchhoff integral where contribution from all points on the illuminated surface are accounted for. In addition the Kirchhoff approximation used to derive stationary phase results in Eq. (3) assumes that the local curvature radius of the rough surface is much greater than the acoustic wavelength, which may not always be true.

Fig. 10 presents the relative pressure fluctuation as a function of the grazing angle which was measured along the support arch as detailed in Section 2.3 and predicted with the FDTD method (see Section 3.1) for the 6 flow conditions. The relative pressure fluctuation was calculated from the known sound pressures (either predicted with the FDTD method or measured) as suggested in [16]

$$\mu(\mathbf{R}_v) = \sqrt{\frac{\overline{|\delta p(\mathbf{R}_v)|^2}}{|\overline{p(\mathbf{R}_v)}|^2}}, \quad (9)$$

where $\overline{p(\mathbf{R}_v)}$ is the mean sound pressure at the position \mathbf{R}_v and $\delta p(\mathbf{R}_v) = p(\mathbf{R}_v) - \overline{p(\mathbf{R}_v)}$ is the fluctuating component of the sound pressure $p(\mathbf{R}_v)$ at the position \mathbf{R}_v . The choice of the relative pressure fluctuations was made to ensure that any potential drift in the amplitude of the 43 kHz acoustic signal radiated by the piezoelectric transducer and in the microphone sensitivity affected by the presence of humid air are compensated for so that the data can be used for the comparison with the predictions obtained with the FDTD method.

Table 2 presents the relative error between the absolute values of the mean sound pressure predicted with FDTD model and measured with the described experimental setup. The relative error for each of the 6 flow conditions was calculated as

$$\varepsilon_{FDTD} = \frac{\sum_v v |\overline{p(\mathbf{R}_v)} - \overline{p_m(\mathbf{R}_v)}|}{\sum_v |\overline{p_m(\mathbf{R}_v)}|}. \quad (10)$$

The results presented in Fig. 10 and in Table 2 suggest that the agreement between the predicted and measured data is within 22.3%. The higher difference of 22.3% is observed for condition 1 (40 mm flow depth). This condition corresponds to the smallest value of the Froude number $Fr = 0.36$, which belongs to a sub-critical regime in which the turbulence-generated gravity-capillary waves do not remain stationary, but disperse in the streamwise and lateral directions resulting in 3-dimensional

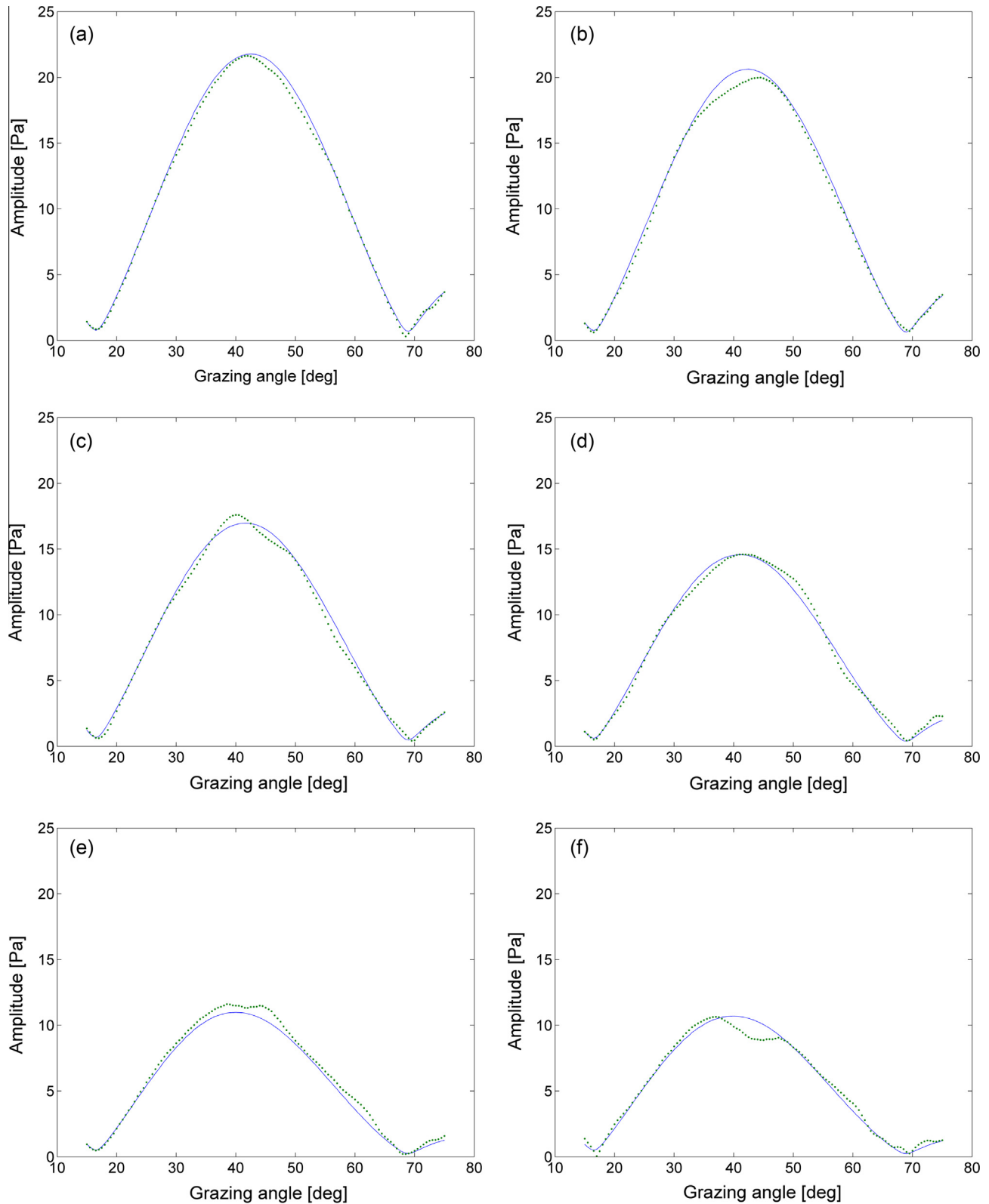


Fig. 9. Comparison of the amplitude (absolute value) of the mean sound pressure scattered by the rough flow surface. Solid line – stationary phase approximation, dots – FDTD model. (a)–(f): Conditions 1–6 (see Tables 1 and 2).

effects which are not captured by either the model or with the adopted LIF experimental setup. Another reason for this discrepancy is the fact that the directivity pattern for the predicted pressure fluctuation is offset by approximately 3–4° with respect to that measured in the experiments (see Fig. 10(a)). This can be

caused by the inaccuracies in setting up the orientation of the highly directional ultrasonic transducer and in controlling of the elevation of the arch above the mean water level. It is easy to illustrate for condition 1 that shifting of the predicted directivity pattern by 3.5° toward the larger angles results in $\varepsilon_{FDTD} = 11.0\%$

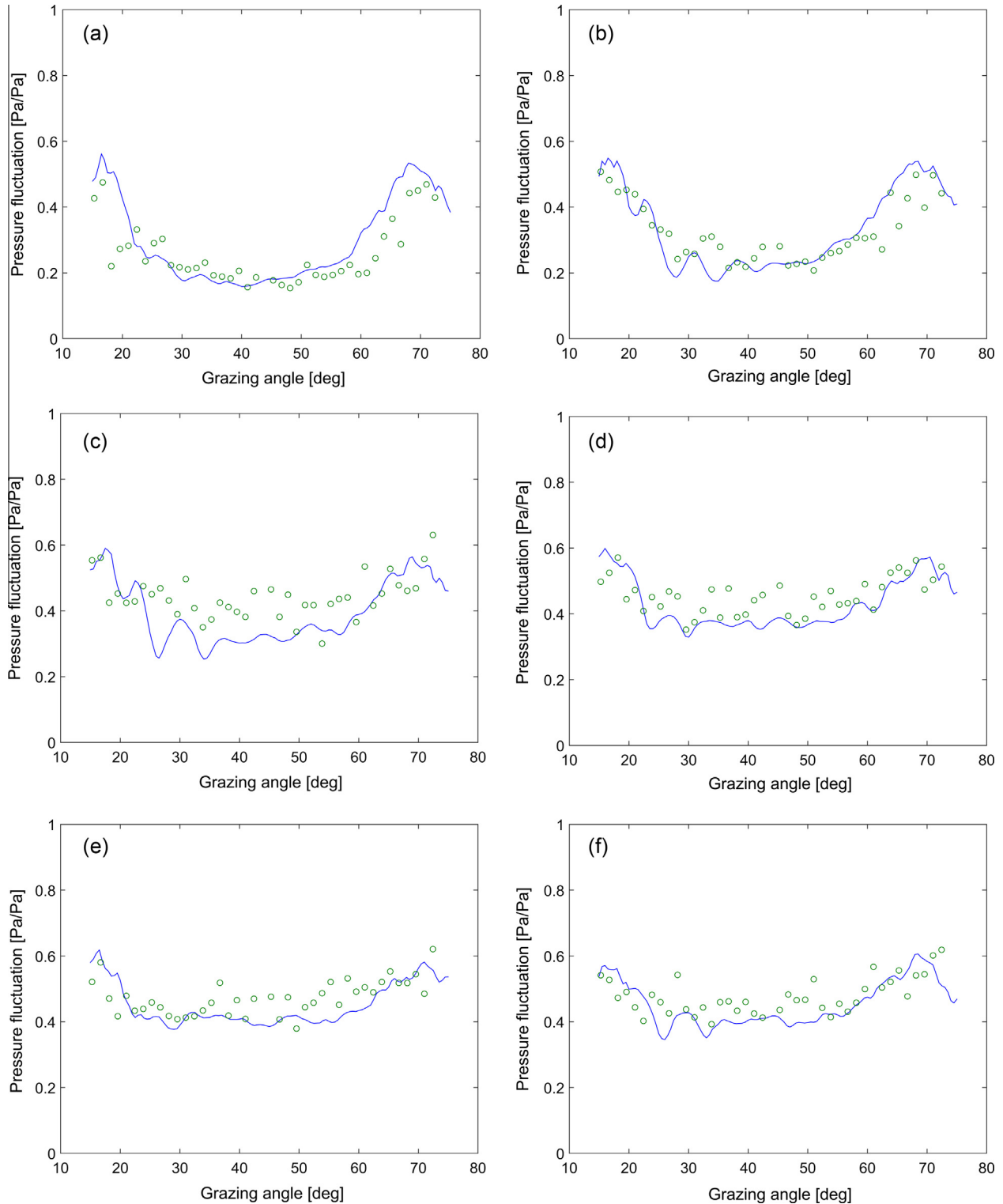


Fig. 10. Relative pressure fluctuation as a function of the grazing angle. Solid line – FDTD predictions, circles – measured data. (a)–(f): Conditions 1–6 (see Tables 1 and 2).

(vs $\varepsilon_{FDTD} = 19.1\%$ without shifting) if the error is calculated for angles above 25° . For the other flow conditions the error is relatively small except for condition 3 (60 mm flow depth) for which the error is $\varepsilon_{FDTD} = 17.5\%$. For these conditions the model generally underpredicts the pressure fluctuation which can relate to the fact that the roughness pattern in the model had to be made quasi-periodic because of the limit in the width of the spatial window within which the adopted LIF system was able to operate. This phenomenon can also be explained by the 3-D scattering effects which

contributed to the measured scattered pressure from surface features being outside the central plane in which the measurements and predictions were performed.

5. Conclusions

In this work the instantaneous elevation of the dynamically rough surface of a turbulent, open channel flow in a rectangular

flume was captured with the method of laser induced fluorescence (LIF). The ability of this surface to scatter a harmonic acoustic wave was studied experimentally and predicted with a two-dimensional FDTD model. The results of FDTD modelling of the scattering of a harmonic acoustic signal by a dynamically rough flow surface suggest that the model is able to predict the directivity of the relative sound pressure fluctuation with the maximum mean error of 22.3%. The maximum difference between the measured and predicted directivity patterns are for condition 1 which corresponds to the 40 mm deep flow with the mean velocity of 0.23 m/s. The most accurate prediction was obtained for condition 5, which corresponds to 80 mm deep flow with the velocity of 0.57 m/s. The possible sources of error here are the difference between the actual and assumed directivity of the source, accuracy in the source positioning and the neglect of 3-dimensional scattering effects in the model which can be attributed to the complex dispersion of 3-dimensional patterns of turbulence-generated gravity-capillary waves. Also, it was not possible to reproduce exactly the actual surface roughness pattern over the whole length of the flow surface used in the model because of the spatial limitation in the adopted LIF fluorescence method.

The directivity of the scattered acoustic pressure predicted by the FDTD model was compared against that predicted with the stationary phase approximation method. There was a close agreement between the two methods with the maximum error of 3.03% in the case of condition 8. This error is likely to be attributed to the fact that the FDTD model is able to predict more accurately the complexity in the directivity of the scattered sound pressure than the stationary phase approximation for a given set of instantaneous surface elevations. These results suggest that it is possible to determine accurately and non-invasively the mean roughness height of the dynamically rough surface of an open channel flow.

Previous works [5,6] have shown that the pattern of the dynamically rough surface in an open channel flow can be related to key flow characteristics such as the flow velocity and depth, and to the underlying hydraulic process, such as hydraulic roughness and turbulence scale and intensity. In this respect, the novelty of the presented work is in the use of the real LIF data and FDTD method to predict the directivity of the sound pressure scattered by a dynamically rough flow surface. Alternatively, a measured directivity pattern could therefore be used to infer the surface pattern characteristics remotely, which in turn can be related to the flow conditions. The ability to relate the surface roughness and the sound pressure scattered by this roughness is significant therefore, because it can enable a non-invasive means of remote flow monitoring. This can facilitate better control and management of processes occurring in natural river flows and in urban drainage systems.

Acknowledgements

The authors would like to acknowledge the funding from the UK's Engineering and Physical Sciences Research Council (Grant EP/G015341/1) for the support of the experimental part of this work. The authors are grateful to Prof. Simon Tait (University of Sheffield) for his advice on the laser induced fluorescence experiment and to Mr. Nigel Smith (University of Bradford) for his contribution to the development of the experimental facilities used in this project.

References

- [1] SBRI Competition. InnovateUK, Non-intrusive river flow measurement; 2014. <https://sbri.innovateuk.org/competition-display-page/-/asset_publisher/E809e7RZ5ZTz/content/non-intrusive-river-flow-measurement/1524978 [last accessed on 30/11/2015].
- [2] Jensen KD. Flow measurements. In: ENCIT2004 – 10th Brazilian cong thermal sci eng, November 29–December 03, 2004. Rio de Janeiro, RJ, Brazil.
- [3] Blenkinsopp CE, Turner IL, Allis MJ, Peirson WL, Garden LE. Application of LiDAR technology for measurement of time-varying free-surface profiles in a laboratory wave flume. *Coast Eng* 2012;68:1–5.
- [4] Irish JL, Wozencraft JM, Cunningham AG, Giroud C. Nonintrusive measurement of ocean waves: LiDAR wave gauge. *J Atmos Ocean Technol* 2006;23:1559–72.
- [5] Horoshenkov KV, Nichols A, Tait SJ, Maximov GA. The pattern of surface waves in a shallow free surface flow. *J Geophys Res: Earth Surf* 2013;118(3):1864–76.
- [6] Nichols A. The interaction mechanism of airborne acoustic fields with turbulent shallow flows. PhD Thesis, University of Bradford; March 2014.
- [7] Alpers W. Theory of radar imaging of internal waves. *Nature* 1985;314(6008):245–7.
- [8] Thorsos EI. The validity of the Kirchhoff approximation for rough surface scattering using a Gaussian roughness spectrum. *J Acoust Soc Am* 1988;83(1):78–92.
- [9] Melcher NB et al. River discharge measurements by using helicopter-mounted radar. *Geophys Res Lett* 2002;29(22):2084.
- [10] Van Renterghem T. Efficient outdoor sound propagation modelling with the finite-difference time-domain (FDTD) method: a review. *Int J Aeroacoust* 2014;13(5–6):385–404.
- [11] Heimann D, Karle R. A linearized Euler finite-difference time-domain sound propagation model with terrain-following coordinates. *J Acoust Soc Am* 2006;119:3813–21.
- [12] Dragna D, Blanc-Benon P, Poisso F. Time-domain solver in curvilinear coordinates for outdoor sound propagation over complex terrain. *J Acoust Soc Am* 2013;133:3751–63.
- [13] Botteldooren D. Finite-difference time-domain simulation of low-frequency room acoustic problems. *J Acoust Soc Am* 1995;98(6):3302–8.
- [14] Berenger J. A perfectly matched layer for the absorption of electromagnetic waves. *J Comput Phys* 1994;114:185–200.
- [15] Krynkin A, Horoshenkov KV, Nichols A, Tait SJ. A non-invasive acoustical method to measure the mean roughness height of the free surface of a turbulent shallow water flow. *Rev Sci Instr* 2014;85:114902.
- [16] Bass FG, Fuks IM. Wave scattering from statistically rough surfaces. Oxford: Pergamon; 1979. p. 103.